

Efficient photon-pair emission from a nanostructured resonator and its theoretical description

Michael Poloczek,^{1, *} Alberto Paniate,^{2, *} Attilio Zilli,³ Vitaliy Sultanov,^{1,4} Yigong Luan,³ Tomás Santiago-Cruz,^{1,4} Luca Carletti,⁵ Marco Finazzi,³ Marco Genovese,² Ivano Ruo-Berchera,² Marzia Ferrera,⁶ Andrea Toma,⁶ Francesco Monticone,⁷ Michele Celebrano,³ and Maria Chekhova^{1,4, †}

¹*Friedrich-Alexander-Universität Erlangen-Nürnberg, Staudtstr. 7, 91058 Erlangen, Germany*

²*Quantum metrology and nano technologies division, INRiM, Strada delle Cacce 91, 10135 Torino, Italy*

³*Department of Physics, Politecnico di Milano, 20133 Milan, Italy*

⁴*Max Planck Institute for the Science of Light, Staudtstr. 2, 91058 Erlangen, Germany*

⁵*Department of Information Engineering, University of Brescia, Via Branze 38, 25123 Brescia, Italy*

⁶*Istituto Italiano di Tecnologia, Via Morego 30, Genova 16163, Italy*

⁷*School of Electrical and Computer Engineering, Cornell University, Ithaca, New York, 14850, USA*

Spontaneous parametric down-conversion (SPDC) in subwavelength nonlinear nanostructures is emerging as a promising source of quantum light, owing to its intrinsic multifunctionality and ability to generate versatile and complex quantum states. Despite this growing interest, the physical mechanisms governing photon-pair generation in nanostructures remain only partially understood. In particular, experimental investigations of key emission properties in individual resonators, such as spatial directionality and spectral characteristics, are still lacking, and predictive theoretical frameworks with direct experimental validation have not yet been established. Here we measure, for the first time, the spatial and spectral properties of photon pairs generated via SPDC in a lithium-niobate bullseye nanostructured resonator. Both spatial and spectral properties show a resonant behavior, which we describe within an extended quasi-normal-mode theoretical framework. This comparison with the theory is enabled by photon-pair count rates reaching up to 0.45 Hz/mW, to our knowledge, the highest reported to date for a nanostructured resonator. Our results provide new physical insight into SPDC in nanostructures and represent an important step toward predictive design strategies for efficient nanoscale sources of quantum light.

INTRODUCTION

Traditionally, spontaneous parametric down-conversion (SPDC) has been exploited in bulk non-centrosymmetric crystals to generate pairs of entangled photons, commonly referred to as signal (s) and idler (i), with frequencies satisfying energy conservation. Few millimetre-sized crystals yield high efficiencies of SPDC as they provide a large interaction length. However, in recent years, SPDC at the nanoscale has attracted significant interest as a route towards compact and integrable sources of quantum light [1–3]. Beyond miniaturization, the relaxation of phase-matching constraints in nanoscale systems enables intrinsic multifunctionality, allowing for the generation of highly versatile quantum states with broad spectral and angular bandwidths [4, 5], arbitrary and tunable polarization entanglement [6–11], spatial entanglement [12], bi-directional emission [13–15], and more complex quantum-state engineering [16] including the observation of two-photon quantum interference [17]. These capabilities have been demonstrated across a variety of nanophotonic platforms, including resonant metasurfaces [8, 9, 11–14, 16–19], subwavelength nonlinear films [6, 10, 15, 20, 21], and dielectric nanoresonators [22–24]. Importantly, nanoscale SPDC allows the employment of a broad class of highly nonlinear materials, including emerging platforms such

as van der Waals crystals [25–28] or organic materials like liquid crystals [29].

Despite these advances, nanostructured SPDC sources still face fundamental challenges. Most notably, there is a lack of quantitative description for the key emission properties, including directionality, spectral features, and the generation efficiency. Moreover, a comparison is missing between theoretical predictions and experimental measurements. This hinders systematic device optimization, resulting in low generation efficiencies.

In nanostructured systems, a large number of interdependent variables determine the properties of photon-pair emission. These include the spatial distribution of the pump electric field inside the nonlinear material, the second-order susceptibility tensor $\chi^{(2)}$, the presence of multiple resonant modes at the signal and idler frequencies, and their mutual interference. As a result, emission properties such as directionality and spectral response cannot be adequately described within the traditional analytical frameworks of nonlinear quantum optics [30, 31] and are typically accessible only through full-wave electromagnetic numerical simulations. In this context, most theoretical studies have relied on the correspondence between SPDC and the sum-frequency generation (SFG) [32–35]. Although this approach is widely adopted, it provides limited physical insight into the underlying modal interactions, makes the reconstruction of

the full angular and spectral emission cumbersome, and, while it has been experimentally validated in waveguides [36], its validation in nanoresonators and metasurfaces remains only partial. More recently, a theoretical framework based on Green's functions expanded in terms of quasi-normal modes (QNMs) has been developed and applied to SPDC in a single nanoresonator [37, 38]; however, this theory has mainly considered idealized scenarios, neglecting effects such as the presence of a substrate or collection into a single-mode fiber (SMF). Moreover, it has not been compared with experiment.

In this work, we design and fabricate a nanostructured resonator whose high efficiency for SPDC allows us to perform, for the first time, the spatial and spectral measurements of photon-pair emission in different scenarios. Furthermore, we extend the QNM model to account for the substrate and the coupling into an SMF, enabling a direct comparison between theoretical predictions and experimental measurements and providing a partial validation of the model.

DESIGN AND SIMULATION

Our device uses a circular Bragg grating (CBG), also known as bullseye nanoresonator [39–42], and consists of a central cylinder surrounded by a concentric ring with two azimuthal cuts (Fig. 1(a)), designed to suppress radial radiation while supporting controlled vertical out-coupling. It is fabricated of lithium niobate (LN) and has a total radius of 1.3 μm and an inner-cylinder radius of 600 nm with a thickness of 500 nm. We pump the nanoresonator at 725 nm from the air side and collect the generated photon pairs through the substrate.

To analyze the nonlinear quantum response of the CBG resonator, we use the extended QNMs framework. QNMs are the eigenmodes of open, non-Hermitian photonic structures and correspond to the solutions of the source-free, time-harmonic Maxwell equations with complex eigenfrequencies $\tilde{\omega}_m = \omega_m - i\gamma_m$, where ω_m is the resonance frequency and γ_m the radiative leakage rate [43, 44].

The QNMs allow one to retrieve theoretically the main properties of the emitted photon pairs. Assuming an ideal detector, the detected photon-pair rate can be written as [37, 38]:

$$\frac{d^4 N_{\text{pair}}}{dt d\Omega_i d\Omega_s d\omega_s} = \mathcal{C}(\mathbf{r}_i, \omega_p - \omega_s; \mathbf{r}_s, \omega_s) \times \left| \tilde{T}_{is}(\mathbf{r}_i, \omega_p - \omega_s, \mathbf{d}_i; \mathbf{r}_s, \omega_s, \mathbf{d}_s) \right|^2 \quad (1)$$

where

$$\mathcal{C}(\mathbf{r}_i, \omega_p - \omega_s; \mathbf{r}_s, \omega_s) \equiv \frac{8}{\pi\mu_0^2} n_i n_s |\mathbf{r}_i|^2 |\mathbf{r}_s|^2 \frac{(\omega_p - \omega_s)^3 \omega_s^3}{c^6} \quad (2)$$

and

$$\tilde{T}_{is} = \sum_{m,n=1}^{\infty} \xi_{m,n}(\omega_s) \tilde{E}_{m,\mathbf{d}_i}(\mathbf{r}_i) \tilde{E}_{n,\mathbf{d}_s}(\mathbf{r}_s) \quad (3)$$

is the two-photon amplitude, i.e. the probability amplitude to detect the idler and signal photons at far-field points \mathbf{r}_i and \mathbf{r}_s and with polarization vectors \mathbf{d}_i and \mathbf{d}_s , respectively. Here, $\omega_i = \omega_p - \omega_s$ and ω_s denote the frequencies of the idler and signal photons, respectively, with ω_p being the pump frequency. The refractive indices of the medium at the idler and signal frequencies are denoted with n_i and n_s while μ_0 and c are the vacuum magnetic permeability and the speed of light, respectively. The detection rate is expressed per unit of far-field solid angles Ω_i (for the idler photon) and Ω_s (for the signal photon), as well as per unit of signal-photon angular frequency ω_s . The $\tilde{E}_{m,\mathbf{d}_i}(\mathbf{r}_i)$ denotes the far-field component of the electric field of the m -th QNM projected onto the detection polarization \mathbf{d}_i . Each electric field is normalized according to QNMs theory. The summation runs over all QNM pairs (m, n) , with the contribution of each pair weighted by the so-called dispersive modal-overlap coefficient,

$$\xi_{m,n}(\omega_s) = \frac{\mathcal{G}_{m,n}}{\mathcal{S}_{m,n}(\omega_s)}, \quad (4)$$

with

$$\mathcal{G}_{m,n} = \sum_{\alpha,\beta,\gamma} \int d\mathbf{r}_0 \chi_{\alpha\beta\gamma}^{(2)}(\mathbf{r}_0) \tilde{E}_{m,\alpha}(\mathbf{r}_0) \tilde{E}_{n,\beta}(\mathbf{r}_0) E_{p,\gamma}(\mathbf{r}_0) \quad (5)$$

and

$$\mathcal{S}_{m,n}(\omega_s) = (\omega_p - \omega_s - \tilde{\omega}_m) \tilde{\omega}_m (\omega_s - \tilde{\omega}_n) \tilde{\omega}_n. \quad (6)$$

In particular, $\mathcal{G}_{m,n}$ quantifies the spatial overlap between the nonlinear susceptibility tensor $\chi^{(2)}$, the QNM fields $\tilde{\mathbf{E}}_m$ and $\tilde{\mathbf{E}}_n$ along directions α and β , and the pump field \mathbf{E}_p along direction γ . Meanwhile, the spectral factor $\mathcal{S}_{m,n}(\omega_s)$ accounts for the complex detuning between the generated photon frequencies (ω_i, ω_s) and the QNM eigenfrequencies $(\tilde{\omega}_m, \tilde{\omega}_n)$, thereby determining the spectral and modal selectivity of SPDC.

Here, we achieve a high efficiency of photon-pair generation by satisfying three key physical conditions: (i) the presence of a mode exhibiting strong far-field directionality along the x -axis, which enhances collection through the optical system; (ii) a significant spatial overlap between the modal field and the pump field \mathbf{E}_p , which enhances the nonlinear coupling strength (5); and (iii) an eigenfrequency close to the degenerate SPDC frequency, which reduces the detuning in Eq. (6).

In particular, simulations of the CBG structure, on an infinitely extended glass substrate reveal, among the supported modes, a strongly directional QNM, labeled as

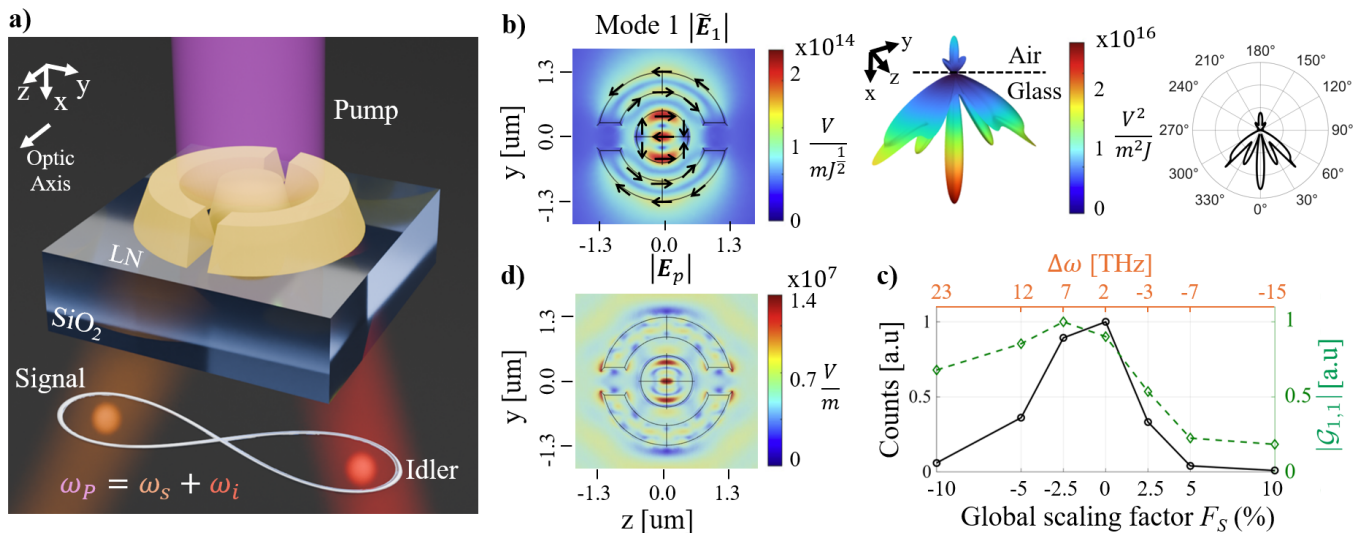


FIG. 1. *Spontaneous parametric down-conversion (SPDC) in a lithium niobate (LN) nanostructured resonator.* (a) Conceptual picture of the entangled photon pair generated by the nanoresonator. (b) Near-field distribution (left panel) and far-field radiation pattern $|\vec{E}|^2$ (right panel, 3D and polar visualization on the $x - y$ plane) of the chosen quasi-normal mode QNM₁. The black arrows indicate the direction of the electric field inside the resonator. (c) Simulated normalized rate of coincidences as a function of the lateral scaling parameter F_S . The factor F_S affects the detuning $\Delta\omega = (\omega_1 - \omega_{\text{deg}})/(2\pi)$ between the eigenfrequency ω_1 of QNM₁ and the degenerate angular frequency ω_{deg} , as well as the spatial overlap $\mathcal{G}_{1,1}$, shown with the green curve. (d) Pump electric field $|E_p(\mathbf{r})|$ inside the resonator, calculated for a plane wave with the intensity $I_0 = 10^9 \text{ W/m}^2$ incident from the resonator side and polarized along the z -axis.

QNM₁. Its near-field distribution and far-field radiation pattern (calculated from the near field with the open-source program RETOP [45]) are shown in the left and right panels of Fig. 1(b), respectively. The mode is normalized according to the procedure described in Ref. [44]. This mode exhibits a pronounced radiation lobe directed into the substrate and aligned with the pump propagation direction, thereby enhancing the collection efficiency.

Conditions (ii) and (iii) are jointly satisfied by the mode and geometry of the CBG nano-resonator. First, in the near field (Fig. 1 (b)), the enhanced electric field of QNM₁ is polarized along the optic axis z of LN, and therefore couples with the largest element $\chi_{zzz}^{(2)}$ of the second-order susceptibility tensor, maximizing the nonlinear spatial overlap. Furthermore, the chosen geometrical dimensions favor the generation of SPDC photon pairs. Indeed, Fig. 1 (c) shows the simulated normalized photon-pair generation rate $\frac{dN_{\text{pair}}}{dt}$, obtained by considering only the QNM pair with $m = n = 1$ in Eq. (3) and integrating over the signal and idler solid angles Ω_s, Ω_i , the signal angular frequency ω_s and all possible polarization states of the entangled photons. The count rate is plotted as a function of the scaling factor F_S applied to the lateral resonator dimensions, $F_S = 0$ corresponding to the scaling used in the experiment. Each count rate has been normalized by the resonator volume to account for the change induced by the factor F_S .

Increasing the lateral dimensions of the resonator shifts the QNM eigenfrequency to lower values, and vice versa,

thereby modifying the detuning, $\Delta\omega = (\omega_1 - \omega_{\text{deg}})/(2\pi)$, from the degenerate SPDC frequency $\omega_{\text{deg}} = \omega_p/2$, shown in orange on the upper axis. At small detuning, a high emission rate is expected; however, detuning alone does not fully determine the emission efficiency. Variations of the resonator size also modify the spatial confinement of the mode and its interaction with the pump field, thereby affecting the spatial overlap $|\mathcal{G}_{1,1}|$, shown by the green curve. As a result, even for comparable detuning values (e.g. around 7 THz), the photon-pair count rate can vary significantly due to differences in the spatial overlap between the pump field and the QNM. The experimental geometry lies at the maximum of the simulated count rate, within the resolution of the explored parameter sweep. The spatial distribution of the pump electric field for this best configuration is shown in Fig. 1 (d) and shows a clear overlap with the QNM₁ field, particularly in the central region of the resonator.

In order to compare theoretical results with the experimental measurements, a complete QNM analysis is performed. Fig. 2(a) reports the real parts of the QNM eigenfrequencies together with their corresponding quality factors $Q = \omega_m/(2\gamma_m)$. Fig. 2(b) shows the frequency dependences of the modal-overlap coefficients $\xi_{m,n}$ for nine QNM pairs with the strongest signal-idler overlap. Among them, the strongest overlap is for the pair QNM₁ - QNM₁. Fig. 2 (c) displays two example modes (3 and 8) to illustrate the different near-field distributions and far-field radiation patterns that can arise

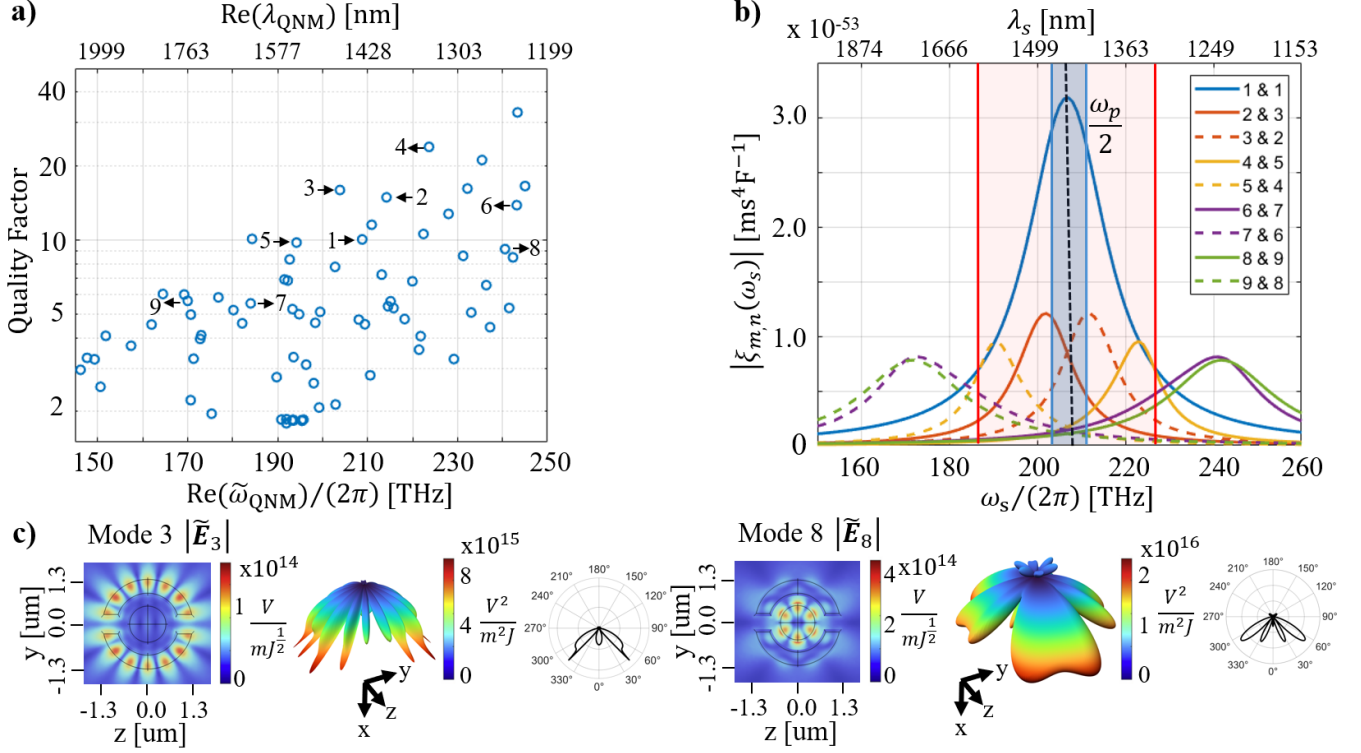


FIG. 2. *Quasi-normal modes of the nano-resonator and modal-overlap coefficient.* (a) Quality factors of all QNMs of the nanostructure, plotted versus the real parts of their eigenfrequencies. Labels indicate the modes exhibiting the largest modal-overlap coefficients $\xi_{m,n}$ across the reported range of frequencies. (b) Modal-overlap coefficients $\xi_{m,n}(\omega_s)$ for the nine QNM pairs with the highest peak values. The vertical dashed line marks the degenerate frequency. The red and blue shaded regions indicate the two frequency collection ranges used in the measurements shown in Fig. 4. (c) Near-field and far-field distributions of two representative modes, 3 and 8, illustrating their different far-field patterns and intensities.

in the resonator. Considering all QNM pairs and their modal overlap coefficients, the final spatial and spectral properties are simulated and compared with the experimental measurements.

EXPERIMENT

The CBG nano-resonator, whose scanning-electron micrograph (SEM) is shown in Fig. 3 (a), was fabricated via focused ion beam (FIB) milling (FEI, dual-beam Helios Nanolab 650) of a commercially available x-cut 500 nm LN film on a fused silica substrate with thickness of 500 μm [46]. Patterning throughout the entire thickness was performed by using Ga^+ ions emitted with a current of 0.77 nA and accelerated by a voltage of 30 kV. After initial experimental characterization through second-harmonic generation, we turned to SPDC measurements.

Fig. 3 (b) presents a schematic of the experimental setup. The central panel depicts the main detection configuration, while the two upper insets illustrate the modifications employed to characterize the spatial and spectral properties of the SPDC emission.

The nano-resonator was pumped from the air-side by a continuous-wave laser at 725 nm whose power was adjusted using a half-wave plate (HWP) and a Glan-Taylor prism. A second HWP adjusted the polarization along the LN optic axis. The pump beam was focused onto the CBG by lens L1 with a focal length of 11 mm, producing a focal spot of approximately 5 μm at $\frac{1}{e^2}$ of the power. The emitted light was collimated by a second lens (L2) with a high numerical aperture (NA=0.7) and a focal length of 3.1 mm. A cascade of long-pass spectral filters with cut-on wavelengths at 850 nm, 950 nm, 1100 nm, and 1300 nm suppressed the residual pump and isolated the SPDC emission. The filtered signal was coupled into a single-mode fiber (SMF-28) and divided into two paths using a 50:50 fiber beam splitter, each connected to a superconducting nanowire single-photon detector (SNSPD), where coincidence events were recorded with a time tagger. This experimental configuration, equivalent to the Hanbury Brown-Twiss detection scheme, was used to measure the pair coincidence rate. Fig. 3(c) shows the distribution of the delay between photon detection times by the two detectors, acquired with a pump power of 10 mW. The pronounced peak around

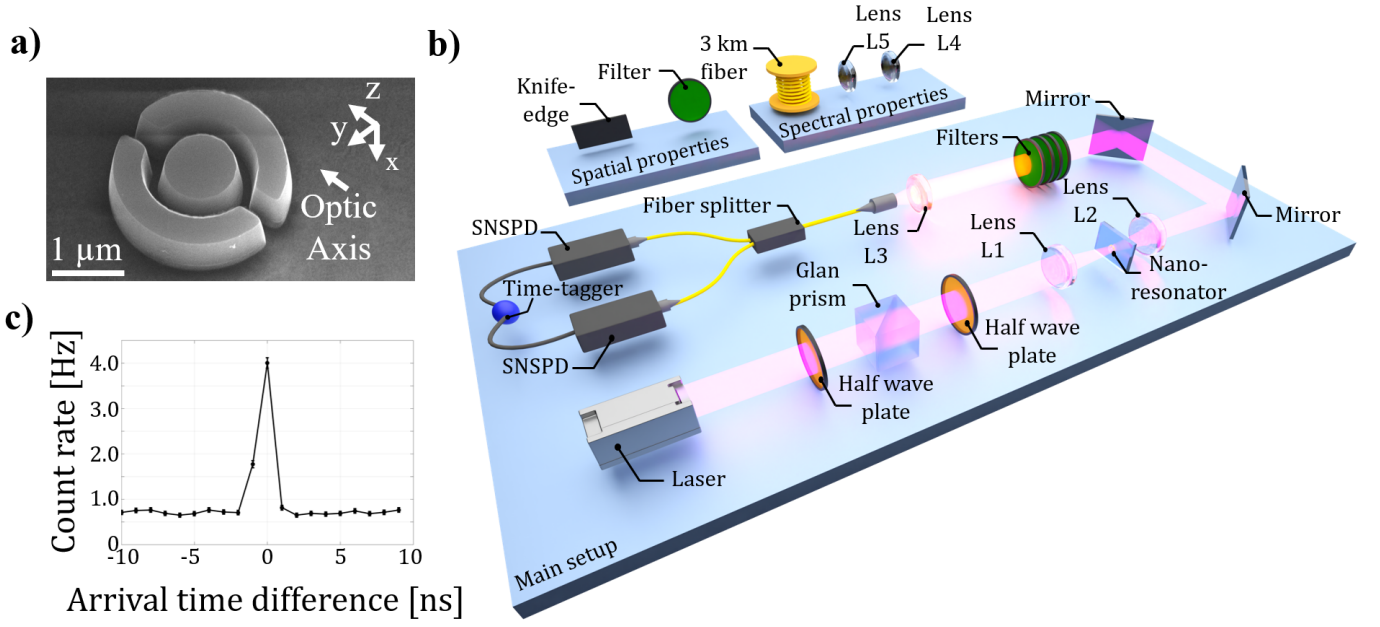


FIG. 3. *Experimental implementation of SPDC in the nano-resonator* (a) SEM picture of the nano-resonator at an intermediate stage of the nano-fabrication process. (b) Schematic view of the experimental setup. The continuous-wave laser power and polarization are controlled using two half-wave plates (HWPs) and a Glan–Taylor prism, and the beam is focused onto the nano-resonator by lens L1. The emitted light is collimated by lens L2. After spatial filtering, the beam is fed into a single-mode fiber by lens L3, and photon-pair coincidences are recorded using superconducting nanowire single-photon detectors (SNSPDs). Spatial properties are measured both with and without spectral filtering around the degenerate wavelength. Spectral properties are characterized by inserting a dispersive fiber after L3 and by introducing a $2\times$ magnifying system composed of lenses L4 and L5. (c) The distribution of the photon arrival time difference, with an incident power of 10 mW, demonstrating a coincidence peak due to the detection of photon pairs.

the zero delay reveals photon pairs generated by the CBG resonator. The total rate of pair detection per pump power is 0.45 Hz/mW, obtained by summing the counts around zero time delay and subtracting the accidentals counts, measured at large time delays. The count rate exceeds the values obtained for other nano- and microresonators [22–24] by more than an order of magnitude.

To characterize the spatial properties of the SPDC emission, we implemented knife-edge scanning before lens L3. By recording the number of coincidences as a function of the knife edge position, we retrieved the angular spectrum of SPDC emission. Two measurement conditions were considered: one collecting the full SPDC bandwidth (approximately 1340 – 1580 nm), and the second one, targeting the resonance region at the degenerate wavelength, by inserting an additional band pass filter (BF) centered at 1450 nm with a full width at half maximum (FWHM) of 50 nm. Both regions are highlighted in Fig. 2 (b) with red and blue areas.

Fig. 4(a) compares the experimentally measured coincidence rates as a function of the knife-edge position with the corresponding simulated results. The blue points represent the normalized experimental counts obtained using the BF centered at the degenerate wavelength, while the red points correspond to measurements without the

BF. The data are fitted using an error function of the form $\text{erf}(x/m)$, where x denotes the knife-edge displacement and m characterizes the slope of the dependence. This fitting model is justified by the fact that coupling into the SMF effectively selects an approximately Gaussian spatial profile of the SPDC emission. The resulting fits are shown as solid blue and red curves for the two measurement conditions. The obtained values of the experimental slope m are: $m_{\text{red}} = (0.69 \pm 0.03)$ mm; $m_{\text{blue}} = (0.49 \pm 0.06)$ mm.

An equivalent procedure is applied to the simulated data. To account for realistic experimental conditions, Eqs. (1–6) are extended to include photon collection through a lens and coupling into the SMF. To this end, we model the fiber mode by a Gaussian profile $\phi(\mathbf{r}) = \frac{1}{\sigma\sqrt{\pi}} \exp\left(-\frac{|\mathbf{r}|^2}{\sigma^2}\right)$, where the mode radius σ is determined by the parameters of the fiber used in the experiment. The detected photon-pair count rate is calculated as

$$\frac{dN_{\text{pair}}}{dt} = \int d\omega_s \int_{\text{NA}} d\Omega_i \int_{\text{NA}} d\Omega_s \phi(\mathbf{r}_i) \phi(\mathbf{r}_s) \times \mathcal{C} \left| \tilde{T}_{is}(\mathbf{r}_i, \omega_p - \omega_s, \mathbf{d}_i; \mathbf{r}_s, \omega_s, \mathbf{d}_s) \right|^2, \quad (7)$$

where the variables entering the prefactor \mathcal{C} have been omitted for brevity. The integration runs only within the

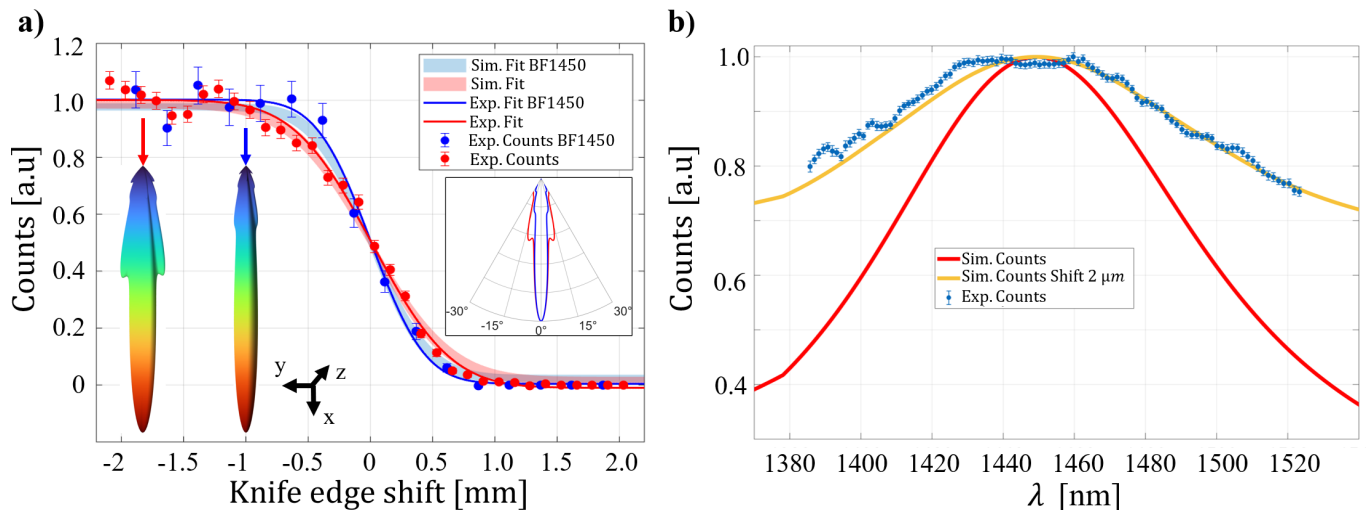


FIG. 4. *Spatial and spectral properties of emission.* (a) Directionality of the emitted photon pairs measured using knife-edge scans. Blue experimental points, fitted by the blue curve, are acquired with a 50 nm bandpass filter centered at the resonance (degenerate) wavelength. Red points, fitted by the red curve, are acquired with a broader detection bandwidth 1340 – 1580 nm. The shaded regions represent the simulated knife-edge scans, with the 95% confidence intervals of the fit. The insets show the far-field coincidence count rate distributions for both cases in 3D and in the plane $x - y$, computed with an account for the limited NA of the collection optics and the SMF. (b) Spectrum of the photon pairs. The experimental points are shown in blue and the simulated spectrum, in red. The yellow curve represents the simulated spectrum when a shift of $2\ \mu\text{m}$ between the center of the SPDC emission and the center of the Gaussian mode of the SMF, considered at the tip.

angles allowed by the NA of the lens. The corresponding fit results are shown as shaded regions indicating the 95% confidence intervals, demonstrating good agreement between experiment and simulation. The obtained parameters of the simulated curves are $m_{\text{red}} = (0.76 \pm 0.02)$ mm; $m_{\text{blue}} = (0.51 \pm 0.02)$ mm. They are in a good agreement with the parameters of the experimental points fit. The insets of Fig. 4(a) display the corresponding 3D and polar far-field distributions of photon-pair rates, computed by accounting for the finite NA of the collection optics and the SMF used in the measurements. These insets highlight the slightly different far-field angular distributions associated with the degenerate and broadband photon-pair contributions.

Both the experimental data and the simulations show that photon pairs generated close to the degenerate wavelength exhibit a slightly narrower knife-edge profile compared to photon pairs collected over a broader spectral range. In bulk SPDC sources, such a behavior can be explained by phase-matching conditions, which impose a wavelength–angle correlation between the emitted photons. However, in thin-film and nano-resonator SPDC sources with subwavelength thickness these constraints are largely relaxed. While in thin films this relaxation leads to no significant difference in the knife-edge scans, in nano-resonators the presence of resonant modes introduces a correlation between the spectral and spatial emission properties, resulting in two different slopes in the knife-edge scans. In particular, photon pairs generated near degeneracy are dominated by the contribution

of QNM_1 , whose far-field emission is highly directional. Applying a BF centered around the eigenfrequency of QNM_1 therefore selectively isolates this contribution, resulting in a sharper knife-edge transition. By contrast, when the full SPDC spectrum is collected, additional QNMs with different eigenfrequencies and spatial radiation patterns contribute to the emission, leading to a broader overall spatial profile.

To investigate the spectral properties of the SPDC emission, two lenses were introduced in front of lens L3 to magnify the far-field pattern by a factor of two, thereby improving the angular selectivity and enabling isolation of the directional emission associated with QNM_1 . In addition, a 3 km dispersive optical fiber was inserted in the detection path to temporally stretch the photon wavepackets through group-velocity dispersion [47]. This wavelength-to-time mapping allows the spectral distribution of the SPDC photons to be retrieved by measuring the coincidence distribution over the arrival-time difference.

Fig. 4(b) compares the measured and simulated SPDC spectra. The experimental data (blue points) are obtained by normalizing the spectrum measured for the nano-resonator to that of an unstructured LN film, thereby compensating for the wavelength-dependent detection efficiency of the SNSPDs. The resulting ratio is smoothed by averaging over fourteen adjacent data points to reduce the noise and enhance the visibility of the resonance feature. In the simulations, the $2\times$ magnification used in the experiment is taken into account.

Unlike the simulated spectrum (red), the experimental spectrum shows a larger width or a considerable background. This discrepancy can be attributed to several factors, including a reduced quality factor of the fabricated resonator due to fabrication imperfections, as well as possible misalignment between the collimated SPDC emission and the SMF. Owing to the high angular selectivity imposed by the experimental configuration, the collected signal is particularly sensitive to small misalignments. In contrast, the simulations assume perfect spatial alignment between the center of SPDC emission and the center of the Gaussian mode of the SMF, resulting in the ideal selection of QNM₁. Even minor misalignments in the experiment can therefore alter the relative modal contributions, leading to a broader measured resonance. This effect is illustrated by the simulation assuming a shift of the fiber mode by $2\ \mu\text{m}$ with respect to the SPDC center emission profile (yellow curve). In this case, the collection efficiency of QNM₁ is reduced, while the contributions of other modes with different spatial profiles become more significant. The resulting spectrum is broader and has a considerable background, providing a plausible explanation for the observed experimental linewidth and partially accounting for the discrepancy between experiment and simulation.

CONCLUSION

In this work, we demonstrate a highly efficient LN nanostructured resonator exhibiting a photon-pair count rate of approximately 4.5 Hz at an excitation power of 10 mW, corresponding to 450 Hz/W. This rate exceeds by more than an order of magnitude the highest value previously reported for a single LN nanostructured resonator, namely 15 Hz/W measured from an LN microcube [23], which itself already improved by about one order of magnitude over the first nano-cylinder demonstration [22]. The comparison becomes even more significant when accounting for the different resonator volumes. The CBG nano-resonator has an estimated volume of $\sim 1.75\ \mu\text{m}^3$, compared to $\sim 46.7\ \mu\text{m}^3$ for the LN microcube, yielding an overall volume-normalized efficiency improvement approaching three orders of magnitude. For applications where the photon-pair generation rate per unit spectral bandwidth is a relevant figure of merit, the CBG nano-resonator reaches a spectral brightness of approximately 1.3 Hz/(W · nm), compared to $\sim 0.12\ \text{Hz}/(\text{W} \cdot \text{nm})$ reported for the LN microcube.

The observed high efficiency has been understood in terms of several key aspects of the nonlinear process, including the spatial overlap between the pump field and the resonant mode, the spectral detuning from the degenerate SPDC frequency, and the coupling efficiency into the SMF. While the investigated geometry already satisfies these conditions to a good approximation, further

improvements are expected through systematic optimization of the geometrical parameters or the adoption of inverse-design strategies [48].

This work extends the QNMs framework to realistic experimental scenarios and provides, to our knowledge, the first experimental test of its predictions for both spatial and spectral properties of SPDC emission from a single nano-resonator. At the same time, the present study should be regarded as a first step toward a fully predictive design of nano-scale SPDC sources. Although this preliminary validation is encouraging, further experimental and theoretical investigations are required to assess the robustness and generality of the theoretical framework. In particular, further characterization of spatial, spectral, and polarization properties with different nano-resonators and metasurfaces together with further studies of SMF collection and projection will be essential to fully evaluate the capabilities and limitations of both the modelling approach and the overall nano-scale SPDC sources.

ACKNOWLEDGMENTS

A.P. thanks Dr. Angelo Angelini for providing access to the workstation used for most of the simulations and ISSNAF for enabling the collaboration with F.M.; A.P., I.R. and M.G. acknowledge funding by NATO SPS G6026. The work of M.P. was supported by the German Academic Scholarship Foundation. A.P. and M.Ch. acknowledge funding by European Research Council (Project 101199215 — MultiFlaQS).

AUTHOR CONTRIBUTIONS

M.P. and V.S. performed the experimental measurements, with guidance from M.Ch and T.S. M.P and A.Z. contributed to the design of the nano-resonator, with guidance from M.Ce. and M.Fi. A.P. carried out the numerical simulations with support from F.M., I.R., and M.G. A.Z. and Y.L. performed the second-harmonic-generation measurements of the nano-resonator, with assistance from M.Ce. and M.Fi. L.C. conducted preliminary simulations of the resonator. M.Fe. and A.T. fabricated the nano-resonator. A.P. wrote the manuscript with contributions from all authors.

CONFLICT OF INTEREST

The authors declare no conflicts of interest.

* These authors contributed equally to this work.

† maria.chekhova@mpl.mpg.de

- [1] F. Ding and S. I. Bozhevolnyi, *Advances in quantum meta-optics*, *Materials Today* **71**, 63 (2023).
- [2] S. A. Schulz, R. Oulton, M. Kenney, A. Alù, I. Staude, A. Bashiri, Z. Fedorova, R. Kolkowski, A. F. Koenderink, X. Xiao, et al., *Roadmap on photonic metasurfaces*, *Applied Physics Letters* **124** (2024).
- [3] J. Ma, J. Zhang, J. Horder, A. A. Sukhorukov, M. Toth, D. N. Neshev, and I. Aharonovich, *Engineering quantum light sources with flat optics*, *Advanced Materials* **36**, 2313589 (2024).
- [4] C. Okoth, A. Cavanna, T. Santiago-Cruz, and M. V. Chekhova, *Microscale generation of entangled photons without momentum conservation*, *Physical review letters* **123**, 263602 (2019).
- [5] C. Okoth, E. Kovlakov, F. Bönsel, A. Cavanna, S. Straupe, S. Kulik, and M. Chekhova, *Idealized Einstein-Podolsky-Rosen states from non-phase-matched parametric down-conversion*, *Physical Review A* **101**, 011801 (2020).
- [6] V. Sultanov, T. Santiago-Cruz, and M. V. Chekhova, *Flat-optics generation of broadband photon pairs with tunable polarization entanglement*, *Optics Letters* **47**, 3872 (2022).
- [7] J. Ma, J. Zhang, Y. Jiang, T. Fan, M. Parry, D. N. Neshev, and A. A. Sukhorukov, *Polarization engineering of entangled photons from a lithium niobate nonlinear metasurface*, *Nano Letters* **23**, 8091 (2023).
- [8] J. Noh, T. Santiago-Cruz, V. Sultanov, C. F. Doiron, S. D. Gennaro, M. V. Chekhova, and I. Brener, *Quantum pair generation in nonlinear metasurfaces with mixed and pure photon polarizations*, *Nano Letters* **24**, 15356 (2024).
- [9] J. Ma, T. Fan, T. Haggren, L. V. Molina, M. Parry, S. Shinde, C. McManus-Barrett, J. Zhang, R. C. Morales, F. Setzpfandt, et al., *Nonlinearity symmetry breaking for generating tunable quantum entanglement in semiconductor metasurfaces*, *Science Advances* **11**, eadu4133 (2025).
- [10] H. Liang, T. Gu, Y. Lou, C. Yang, C. Ma, J. Qi, A. A. Bettiol, and X. Wang, *Tunable polarization entangled photon-pair source in rhombohedral boron nitride*, *Science Advances* **11**, eadt3710 (2025).
- [11] W. Jia, G. Saerens, Ü.-L. Talts, H. Weigand, R. J. Chapman, L. Li, R. Grange, and Y. Yang, *Polarization-entangled bell state generation from an epsilon-near-zero metasurface*, *Science Advances* **11**, eads3576 (2025).
- [12] J. Zhang, J. Ma, M. Parry, M. Cai, R. Camacho-Morales, L. Xu, D. N. Neshev, and A. A. Sukhorukov, *Spatially entangled photon pairs from lithium niobate nonlocal metasurfaces*, *Science Advances* **8**, eabq4240 (2022).
- [13] C. Son, V. Sultanov, T. Santiago-Cruz, A. P. Anthur, H. Zhang, R. Paniagua-Dominguez, L. Krivitsky, A. I. Kuznetsov, and M. V. Chekhova, *Photon pairs bi-directionally emitted from a resonant metasurface*, *Nanoscale* **15**, 2567 (2023).
- [14] M. A. Weissflog, J. Ma, J. Zhang, T. Fan, S. Lung, T. Pertsch, D. N. Neshev, S. Saravi, F. Setzpfandt, and A. A. Sukhorukov, *Directionally tunable co-and counter-propagating photon pairs from a nonlinear metasurface*, *Nanophotonics* **13**, 3563 (2024).
- [15] Z. Lu, J. Janousek, S. M. Assad, S. Qiu, M. Joshi, Y. Hu, A. Y. Song, C. Wang, M. Suriyage, J. Zhao, and Y. Lu, *Counter-propagating entangled photon pairs from monolayer GaSe*, *Nature Communications* **16**, 9616 (2025).
- [16] T. Santiago-Cruz, S. D. Gennaro, O. Mitrofanov, S. Addamane, J. Reno, I. Brener, and M. V. Chekhova, *Resonant metasurfaces for generating complex quantum states*, *Science* **377**, 991 (2022).
- [17] J. Noh, T. Santiago-Cruz, C. F. Doiron, H. Jung, J. Yu, S. J. Addamane, M. V. Chekhova, and I. Brener, *Fano interference of photon pairs from a metasurface*, *Light: Science & Applications* **14**, 371 (2025).
- [18] T. Santiago-Cruz, A. Fedotova, V. Sultanov, M. A. Weissflog, D. Arslan, M. Younesi, T. Pertsch, I. Staude, F. Setzpfandt, and M. Chekhova, *Photon pairs from resonant metasurfaces*, *Nano letters* **21**, 4423 (2021).
- [19] J. Ma, J. Ren, J. Zhang, J. Meng, C. McManus-Barrett, K. B. Crozier, and A. A. Sukhorukov, *Quantum imaging using spatially entangled photon pairs from a nonlinear metasurface*, *eLight* **5**, 2 (2025).
- [20] T. Santiago-Cruz, V. Sultanov, H. Zhang, L. A. Krivitsky, and M. V. Chekhova, *Entangled photons from subwavelength nonlinear films*, *Optics Letters* **46**, 653 (2021).
- [21] S. Stich, V. Sultanov, T. Blaikie, Q. Shi, Z. Wasilewski, M. A. Belkin, and M. Chekhova, *Thin-film Al_{0.30}Ga_{0.70}As (111) as a ‘flat’ source of high-purity orthogonally polarized entangled photons*, *Optics Express* **34**, 1664 (2026).
- [22] G. Marino, A. S. Solntsev, L. Xu, V. F. Gili, L. Carletti, A. N. Poddubny, M. Rahmani, D. A. Smirnova, H. Chen, A. Lemaître, et al., *Spontaneous photon-pair generation from a dielectric nanoantenna*, *Optica* **6**, 1416 (2019).
- [23] N. M. H. Duong, G. Saerens, F. Timpu, M. T. Buscaglia, V. Buscaglia, A. Morandi, J. S. Müller, A. Maeder, F. Kaufmann, A. S. Solntsev, and R. Grange, *Spontaneous parametric down-conversion in bottom-up grown lithium niobate microcubes*, *Optical Materials Express* **12**, 3696 (2022).
- [24] G. Saerens, T. Dursap, I. Hesner, N. M. Duong, A. S. Solntsev, A. Morandi, A. Maeder, A. Karvounis, P. Regreny, R. J. Chapman, et al., *Background-free near-infrared biphoton emission from single GaAs nanowires*, *Nano Letters* **23**, 3245 (2023).
- [25] Q. Guo, X.-Z. Qi, L. Zhang, M. Gao, S. Hu, W. Zhou, W. Zang, X. Zhao, J. Wang, B. Yan, et al., *Ultrathin quantum light source with van der Waals NbOC₁₂ crystal*, *Nature* **613**, 53 (2023).
- [26] M. A. Weissflog, A. Fedotova, Y. Tang, E. A. Santos, B. Laudert, S. Shinde, F. Abtahi, M. Afsharnia, I. Pérez Pérez, S. Ritter, et al., *A tunable transition metal dichalcogenide entangled photon-pair source*, *Nature Communications* **15**, 7600 (2024).
- [27] L. Kallioniemi, X. Lyu, R. He, A. Rasmita, R. Duan, Z. Liu, and W. Gao, *Van der Waals engineering for quantum-entangled photon generation*, *Nature Photonics* **19**, 142 (2025).
- [28] C. Trovatello, C. Ferrante, B. Yang, J. Bajo, B. Braun, Z. H. Peng, X. Xu, P. K. Jenke, A. Ye, M. Delor, et al., *Quasi-phase-matched up-and down-conversion in periodically poled layered semiconductors*, *Nature Photonics* **19**, 291 (2025).

- [29] V. Sultanov, A. Kavčič, E. Kokkinakis, N. Sebastián, M. V. Chekhova, and M. Humar, Tunable entangled photon-pair generation in a liquid crystal, *Nature* **631**, 294 (2024).
- [30] D. N. Klyshko, *Photons and Nonlinear Optics* (Routledge, 2018).
- [31] N. J. Sorensen, V. Sultanov, and M. V. Chekhova, A simple model for entangled photon generation in resonant structures, *Optics Express* **33**, 13946 (2025).
- [32] M. Parry, A. Mazzanti, A. Poddubny, G. D. Valle, D. N. Neshev, and A. A. Sukhorukov, Enhanced generation of nondegenerate photon pairs in nonlinear metasurfaces, *Advanced Photonics* **3**, 055001 (2021).
- [33] B. Jin, D. Mishra, and C. Argyropoulos, Efficient single-photon pair generation by spontaneous parametric down-conversion in nonlinear plasmonic metasurfaces, *Nanoscale* **13**, 19903 (2021).
- [34] T. Liu, M. Qin, S. Feng, X. Tu, T. Guo, F. Wu, and S. Xiao, Efficient photon-pair generation empowered by dual quasibound states in the continuum, *Physical Review B* **109**, 155424 (2024).
- [35] A. Mazzanti, M. Parry, A. N. Poddubny, G. Della Valle, D. N. Neshev, and A. A. Sukhorukov, Enhanced generation of angle correlated photon-pairs in nonlinear metasurfaces, *New Journal of Physics* **24**, 035006 (2022).
- [36] F. Lenzini, A. N. Poddubny, J. Titchener, P. Fisher, A. Boes, S. Kasture, B. Haylock, M. Villa, A. Mitchell, A. S. Solntsev, et al., Direct characterization of a nonlinear photonic circuit's wave function with laser light, *Light: Science & Applications* **7**, 17143 (2018).
- [37] A. N. Poddubny, I. V. Iorsh, and A. A. Sukhorukov, Generation of photon-plasmon quantum states in nonlinear hyperbolic metamaterials, *Physical review letters* **117**, 123901 (2016).
- [38] M. A. Weissflog, R. Dezert, V. Vinel, C. Gigli, G. Leo, T. Pertsch, F. Setzpfandt, A. Borne, and S. Saravi, Nonlinear nanoresonators for Bell state generation, *Applied Physics Reviews* **11** (2024).
- [39] M. Davanco, M. T. Rakher, D. Schuh, A. Badolato, and K. Srinivasan, A circular dielectric grating for vertical extraction of single quantum dot emission, *Applied Physics Letters* **99** (2011).
- [40] J. Liu, R. Su, Y. Wei, B. Yao, S. F. C. d. Silva, Y. Yu, J. Iles-Smith, K. Srinivasan, A. Rastelli, J. Li, et al., A solid-state source of strongly entangled photon pairs with high brightness and indistinguishability, *Nature nanotechnology* **14**, 586 (2019).
- [41] H. Wang, H. Hu, T.-H. Chung, J. Qin, X. Yang, J.-P. Li, R.-Z. Liu, H.-S. Zhong, Y.-M. He, X. Ding, et al., On-demand semiconductor source of entangled photons which simultaneously has high fidelity, efficiency, and indistinguishability, *Physical review letters* **122**, 113602 (2019).
- [42] A. Barbiero, G. Shooter, T. Muller, J. Skiba-Szymanska, R. M. Stevenson, L. E. Goff, D. A. Ritchie, and A. J. Shields, Polarization-selective enhancement of telecom wavelength quantum dot transitions in an elliptical bullseye resonator, *Nano letters* **24**, 2839 (2024).
- [43] P. T. Kristensen and S. Hughes, Modes and mode volumes of leaky optical cavities and plasmonic nanoresonators, *ACS Photonics* **1**, 2 (2014).
- [44] P. Lalanne, W. Yan, K. Vynck, C. Sauvan, and J.-P. Hugonin, Light interaction with photonic and plasmonic resonances, *Laser & Photonics Reviews* **12**, 1700113 (2018).
- [45] J. Yang, J.-P. Hugonin, and P. Lalanne, Near-to-far field transformations for radiative and guided waves, *ACS photonics* **3**, 395 (2016).
- [46] L. Carletti, A. Zilli, F. Moia, A. Toma, M. Finazzi, C. De Angelis, D. N. Neshev, and M. Celebrano, Steering and encoding the polarization of the second harmonic in the visible with a monolithic linbo3 metasurface, *ACS photonics* **8**, 731 (2021).
- [47] A. Valencia, M. V. Chekhova, A. Trifonov, and Y. Shih, Entangled two-photon wave packet in a dispersive medium, *Physical Review Letters* **88**, 183601 (2002).
- [48] S. Stich, J. Mohajan, D. de Ceglia, L. Carletti, H. Jung, N. Karl, I. Brener, A. W. Rodriguez, M. A. Belkin, and R. Sarma, Inverse design of an all-dielectric nonlinear polaritonic metasurface, *ACS nano* **19**, 17374 (2025).